

Nanostructured Si–C Composites As High-Capacity Anode Material For All-Solid-State Lithium-Ion Batteries**

Stephanie Poetke,^[a, b] Felix Hippauf,^[b] Anne Baasner,^[a, b] Susanne Dörfler,^{*[b]} Holger Althues,^[b] and Stefan Kaskel^[a, b]

Silicon carbon void structures (Si–C) are attractive anode materials for lithium-ion batteries to cope with the volume changes of silicon during cycling. In this study, Si–C with varying Si contents (28–37%) are evaluated in all-solid-state batteries (ASSBs) for the first time. The carbon matrix enables enhanced performance and lifetime of the Si–C composites compared to bare silicon nanoparticles in half-cells even at high loadings of up to 7.4 mAh cm^{-2} . In full cells with nickel-rich NCM ($\text{LiNi}_{0.9}\text{Co}_{0.05}\text{Mn}_{0.05}\text{O}_2$, 210 mAh g^{-1}), kinetic limitations in the anode lead to a lowered voltage plateau compared to NCM

half-cells. The solid electrolyte ($\text{Li}_6\text{PS}_5\text{Cl}$, 3 mS cm^{-1}) does not penetrate the Si–C void structure resulting in less side reactions and higher initial coulombic efficiency compared to a liquid electrolyte (72.7% vs. 31.0%). Investigating the influence of balancing of full cells using 3-electrode ASSB cells revealed a higher delithiation of the cathode as a result of the higher cut-off voltage of the anode at high n/p ratios. During galvanostatic cycling, full cells with either a low or rather high overbalancing of the anode showed the highest capacity retention of up to 87.7% after 50 cycles.

1. Introduction

Global warming, limited availability of fossil fuels as well as the exposition to health-damaging air pollutants arising from road traffic especially in cities require new mobility concepts. Electric vehicles (EV) with batteries as energy storage are a promising alternative to internal combustion engine vehicles.^[1,2-4] Lithium-ion batteries (LIBs), the dominating technology used in portable electronics, are ideally suited for EV due to their high energy and power density.^[2,3,5] However, the energy density of the intercalation-based state-of-the-art LIB with a layered oxide as cathode and graphite as anode is limited.^[6,7]

High-performance anode materials are required to further increase the driving range and shorten the charge times of EV.^[6,8,9] Furthermore, the volatile and flammable liquid electrolytes (LEs) used in conventional LIBs pose safety concerns. All-solid-state batteries (ASSBs) using solid electrolytes (SEs) instead of organic solvents can potentially provide safer LIBs.^[10]

In addition, the mechanical rigidity of SEs may prevent the growth of lithium dendrites and thus enable the use of lithium metal as anode material.^[11] The gravimetric and volumetric capacity of lithium (3860 mAh g^{-1} , 2050 mAh cm^{-3})^[12] is significantly higher than the theoretical capacity of graphite (339 mAh g^{-1} , 747 mAh cm^{-3})^[12] leading to a theoretical increase in energy density of up to 70%.^[11] However, remaining problems like high reactivity of lithium metal, volume expansion during cycling and thermodynamic instability of most electrolytes against lithium metal need to be further addressed.^[7,11] Additionally, formation of lithium dendrites even through glass ceramic solid electrolytes along the grain boundaries can also take place in ASSBs leading to short circuits^[13] and contact loss at the anode/SE interface under high anodic load due to vacancy diffusion limitation induced pore formation.^[14] Ag–C nanocomposite framework layers as anode could be a promising approach to both suppress Li dendrite formation and obtain high energy densities and long cycle life.^[15]

The lithium alloy forming element silicon is another attractive alternative to lithium due to its high gravimetric and volumetric capacity (1857 mAh g^{-1} , 2190 mAh cm^{-3}), low delithiation potential (0.4 V vs. Li/Li^+) and high abundance lowering battery production costs.^[12,16,17,18] Tesla just recently announced that their future battery technology will be based on cheap and abundant silicon anodes.^[19] However, bulk silicon cannot be effectively utilized in a battery. The high volume change of silicon during (de)lithiation of about 300% lead to particle pulverization, loss of electrical contact and an unstable solid electrolyte interphase (SEI), resulting in low coulombic efficiency and permanent capacity decay.^[4,18,20] In order to compensate the volume changes of silicon, several nano-scaled materials such as silicon nanoparticles,^[21,22] nanowires,^[23,24] nanotubes,^[25] and thin films^[26,27] have been developed. It has

[a] S. Poetke, A. Baasner, Prof. Dr. S. Kaskel
Department of Inorganic Chemistry I
Technische Universität Dresden
Bergstraße 66, 01069 Dresden, Germany

[b] S. Poetke, Dr. F. Hippauf, A. Baasner, Dr. S. Dörfler, Dr. H. Althues,
Prof. Dr. S. Kaskel
Department of Surface and Battery Technology
Fraunhofer Institute for Material and Beam Technology (IWS)
Winterbergstraße 28, 01277 Dresden, Germany
E-mail: susanne.doerfler@iws.fraunhofer.de

[**] A previous version of this manuscript has been deposited on a preprint server (DOI: <https://doi.org/10.26434/chemrxiv.14096049>)

 Supporting information for this article is available on the WWW under <https://doi.org/10.1002/batt.202100055>

 © 2021 The Authors. *Batteries & Supercaps* published by Wiley-VCH GmbH. This is an open access article under the terms of the Creative Commons Attribution License, which permits use, distribution and reproduction in any medium, provided the original work is properly cited.

been shown that crystalline silicon nanoparticles with a diameter < 150 nm do not crack^[21] although μm -scaled columnar silicon structures^[27,28] are a viable anode system. To further improve the mechanical stability and the conductivity of the silicon anode, several composites of the silicon nanostructures with carbon,^[18,29] transition metal oxides like TiO_2 ,^[30] metals,^[31] and polymers^[32] have been designed. However, these composites have mostly been analyzed as anode material in conventional LIBs with liquid electrolytes yet.

Although encouraging results of nano-scaled silicon anodes with liquid electrolytes regarding capacity, initial coulombic efficiency (ICE), rate capability and capacity retention have been published,^[18,33] safety issues and also higher costs due to the need of electrolyte additives^[34] and special separators^[11,35] are still present in conventional lithium-ion batteries.

Replacing the liquid electrolyte with a SE improves the thermal stability^[11] and partially prevents electrolyte depletion as only lithium ions are mobile^[11,36,37] in the battery cell. Regarding the volume changes of silicon during cycling, the solid-state approach also hinders the permanent formation and growth of the SEI in ASSBs compared to conventional LIBs.^[28,37] In our previous work, we showed that columnar silicon anodes form a stable 2D SEI when in contact with sulfide solid electrolyte which reduces the surface area for side reactions, prevents depletion of the liquid electrolyte that penetrates into even smallest pores of the active material and eventually leads to higher ICE and capacity retention.^[28]

Other studies analyzing silicon as potential high-energy anode for ASSBs in the form of amorphous silicon films,^[37,38] composite electrodes constituted of porous SiNPs, SE and acetylene black^[39] or a particulate anode composed of crystalline silicon nanoparticles prepared by spray deposition^[40] show lithiation capacities of up to $3000 \text{ mAh g}^{-1}_{\text{Si}}$ with a capacity

retention of up to 93% over 100 cycles and good rate capabilities in half-cells. However, full cell studies taking proper balancing into account are rare.

In order to address the issue of the drastic volume changes of silicon during cycling we investigate silicon carbon void structures (Si–C) in this study as anode material for ASSBs both in half-cells vs. lithium and full cells with nickel-rich layered oxide (NCM) as cathode. $\text{Li}_6\text{PS}_5\text{Cl}$ – an argyrodite-type sulfide electrolyte – is used as solid electrolyte. Within the different types of SEs, sulfide solid electrolytes (SSEs) like $\text{Li}_6\text{PS}_5\text{Cl}$ possess ionic conductivities comparable to liquid electrolytes.^[41] Furthermore, SSEs can be compressed at room temperature which enables prototype cell manufacturing.^[42]

Silicon carbon composites have only been rarely analyzed in combination with SEs yet but e.g. nanostructured Si/C fibers in ASSBs deliver a reversible capacity of about 700 mAh g^{-1} over 70 cycles with CEs up to 99.2% in half-cells.^[43] The nanostructured Si–C composites used in this study offering a void between the silicon nanoparticle (SiNP) and the outer carbon shell^[12,44] have already been analyzed in conventional LIBs.^[18] The free volume between the silicon core and the carbon matrix does not only allow a free volume expansion of silicon but the carbon shell also increases the electric conductivity of the anode and the stability of the SEI which forms at the outer carbon shell surface.^[8,12,18,44] To the best of our knowledge, we report here for the first time, nanostructured silicon carbon composite void structures as anodes in all-solid-state Li-ion batteries and their successful implementation into full cells. Similar to liquid electrolytes, the carbon shell can effectively compensate the volume changes of silicon which improves the electrochemical performance compared to bare SiNPs (Figure 1). In contrast to liquid electrolytes, ASSB full cells using the proposed Si–C void anodes in combination with

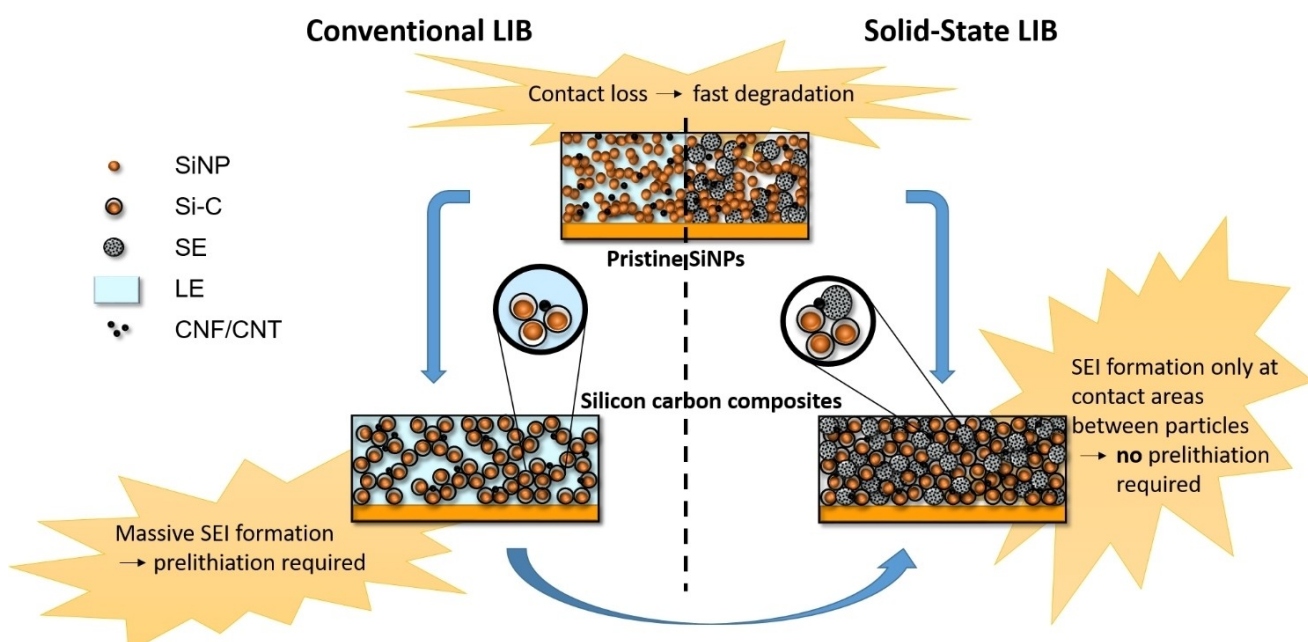


Figure 1. Schematic representation of SiNP (top) and Si–C (bottom) anode in liquid (left) and solid electrolyte (right) Li-ion battery systems.

SEs require no precycling in half-cell vs. lithium.^[18] A crucial advantage is the SE, which cannot penetrate into the entire void structure of the Si–C composite as it would be the case for a liquid electrolyte, causing repeated SEI formation and detrimental (initial) irreversible lithium loss. The SE in contact with Si–C significantly reduces such classical decay mechanisms (Figure 1). Further benefits of ASSBs are high(er) practical areal loadings of the electrodes and a mechanically stabilized SEI by an external pressure.

Herein, Si–C composites with variable Si mass contents are firstly analyzed in half-cells vs. lithium. Subsequently, the Si–C composite with the most promising electrochemical performance is used as active anode material in full cells vs. NCM. Within the full cells, various n/p ratios ranging from 1.1 to 2.0 are electrochemically studied to investigate the influence of the balancing on the cell performance as well as to find an optimal ratio between anode and cathode capacity. Mechanistic insights are provided using an ASSB-3-electrode setup revealing the evolution of the involved electrodes in NCM|SE|Si–C full cells.

2. Results and Discussion

2.1. Structural Characterization of Si–C Composites

Several Si–C composites were synthesized using silicon nanoparticles (SiNPs), polyvinylbutyral (PVB) as void template and sucrose as carbon precursor applying a similar route as previously described.^[18,44] After melt coating PVB on the SiNPs, the sucrose is polymerized via a wet-chemical process around the particles. During pyrolysis, PVB is removed through thermal decomposition whereby voids are formed *in-situ*. However, the void template is not completely eliminated during pyrolysis, especially at lower temperatures, due to the sucrose shell. Presumably, similar to sulfur as template,^[44] complex reactions between PVB residual and polymerized sucrose take place during pyrolysis. Therefore, the resulting carbon content of the Si–C composites is influenced by these complex carbonization processes. As the sucrose to silicon ratio is the same in all syntheses, the different Si to PVB mass ratios adjusted at the beginning of Si–C composite synthesis (Table 1) lead to various final mass fractions of Si, which were determined by combustion analysis (Table 1). In addition, the employed Si particles are not uniform in size or rather the particle size differ for different batches which might also cause unpredictable final carbon to silicon ratios. Hence, the Si–C composites (Si28@C, Si34@C, Si37@C) are named after their respective Si content.

Table 1. Starting PVB:Si mass ratio and estimated Si content of Si–C composites.		
Label	PVB:Si mass ratio	Si content [mass fraction in %]
Si28@C	3:1	28.21
Si34@C	0.5:1	34.45
Si37@C	5:1	36.86

The X-ray diffraction pattern of the Si–C composite with a Si content of 28.21% (Si28@C) shows only a small peak ((002), hexagonal graphite structure) originating from the carbon shell,^[45] but stronger peaks of the cubic face-centered silicon lattice (Figure 2a) proving the presence of crystalline SiNPs.^[39] The peaks at 295 cm⁻¹, 946 cm⁻¹, and the intensive band at 513 cm⁻¹ in the Raman spectra (Figure 2b) origin from crystalline silicon (c-Si).^[46,47] While the peak at 513 cm⁻¹ originates from the scattering of the first-order optical phonon of c-Si, the peaks at 295 cm⁻¹ and 946 cm⁻¹ are due to the scattering of two transverse acoustic and two transverse optical phonons, respectively.^[46] The carbon shell surrounding the c-SiNPs causes the D- (1348 cm⁻¹) and G-band (1594 cm⁻¹).^[48] The carbon matrix surrounding the SiNPs is also visible in the transmission electron microscopy (TEM) images (Figure 2c-d). However, voids are not as clearly visible as compared to other core shell templates^[44] due to the lower contrast in the TEM images which arises from residual carbon derived from PVB in the voids. Hence, the SiNPs, the voids and the carbon shell are not always clearly distinguishable, but this also indicates an intimate contact between carbon and silicon. Similar XRD patterns, Raman peaks and TEM images can also be observed for the Si–C composites Si34@C and Si37@C (Figure S1, Figure S2).

To investigate the morphology of the Si–C composites and compare them to bare SiNPs, the materials were analyzed by scanning electron microscopy (SEM). The SEM images of the commercially available SiNPs show globular, partially aggregated nanoparticles (Figure 3a). The aggregation lowers the surface energy of the nanoparticles and leads to a carbon coating of SiNP agglomerates rather than individual SiNPs as can be seen in the SEM images of the Si–C composites (Figure 3b-d).^[44] Although a homogeneous carbon coating surrounding the crystalline SiNPs is observable for all Si–C composites (Figure 3b-d), the structure differs for the respective PVB:Si mass ratio employed in the synthesis and the resulting Si content.

The Si–C particles of Si34@C (Figure 3c, 60 ± 8 nm) have almost the same diameter as the bare SiNPs (52 ± 5 nm) and are smaller compared to Si37@C (Figure 3d, 64 ± 7 nm) or Si28@C (Figure 3b, 94 ± 16 nm) particles, which is due to the smaller amount of the void template in the synthesis of Si34@C. However, the values should not be overestimated as only a certain area of the sample is analyzed. A higher PVB content in the synthesis (3:1, 5:1) leads to a more compact structure of the Si–C composites. In addition, PVB does not only act as void template but also as carbon source, since the PVB:Si mass ratio also influences the C-content of the composites (Table 1).

Compared to the bare SiNPs, the diameter as well as the degree of agglomeration of the embedded SiNPs beneath the carbon shell increases from Si34@C (PVB:Si=0.5:1) over Si37@C (PVB:Si=5:1) to Si28@C (PVB:Si=3:1) which also leads to the larger diameter of the Si–C agglomerates and decreasing inter-particle distances of the composites in this order.

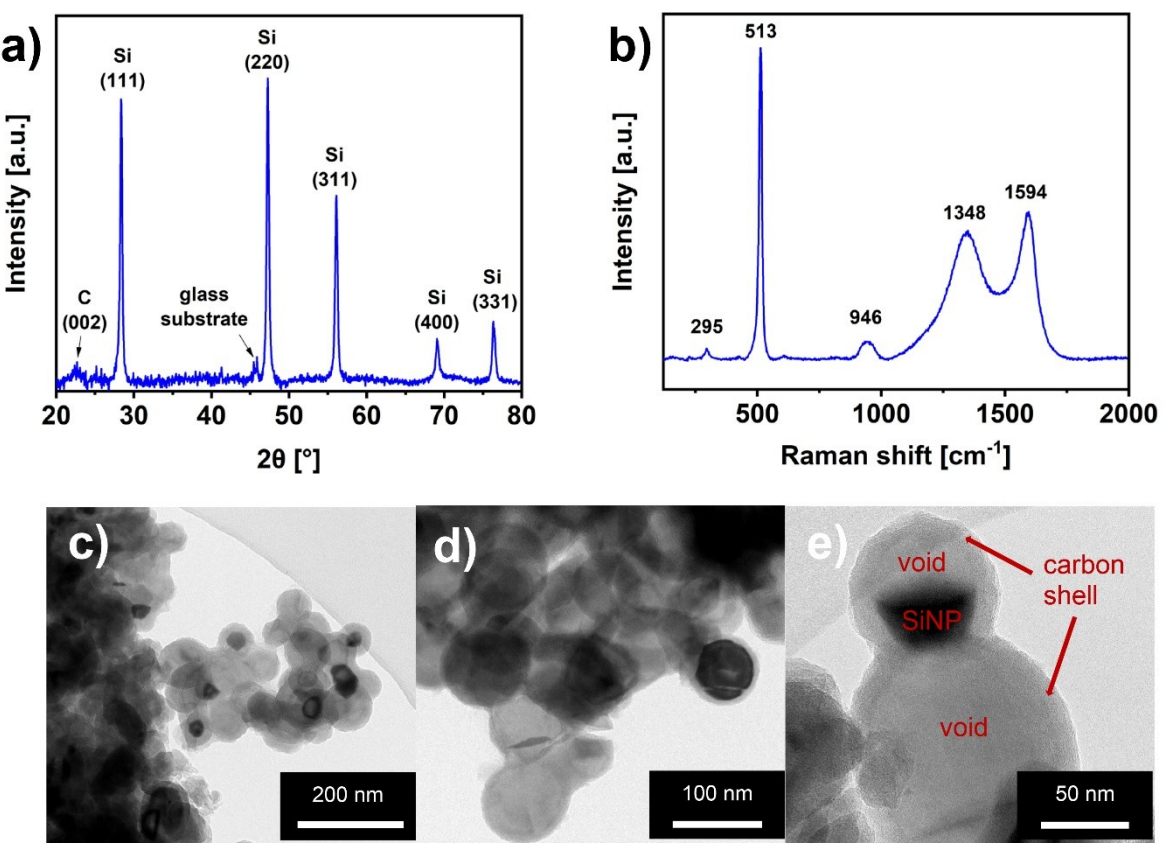


Figure 2. XRD powder pattern (a), Raman spectrum (b) and TEM images (c-e) of the Si–C composite with a Si content of 28% (Si28@C).

2.2. Electrochemical Characterization of Nanostructured Si–C Composites in Half-Cells

For electrochemical testing, the Si–C composite anodes were assembled with Si–C (Si28@C, Si34@C, Si37@C) as active material, Li₆PS₅Cl as solid electrolyte and CNF as conductive additive. Bare SiNPs as well as a Si/C65 mixture containing silicon and carbon nanoparticles in the same Si:C mass ratio as Si37@C are used as reference active materials in order to analyze which impact the carbon void structure surrounding the SiNPs in the Si–C has on the cell performance.

Initially, the lithiation and delithiation mechanism of the Si–C composites were investigated by galvanostatic cycling with potential limitation (GCPL) and cyclic voltammetry (CV). The first lithiation (discharging) starts from c-SiNPs. The flatter voltage profile of the Si–C composite electrodes until around 0.4 V (Figure 4a) as compared to the abrupt descend voltage curve of the bare SiNP electrode (Figure S3a) can be explained with the carbon shell surrounding the SiNPs. The lithium ions have to penetrate the carbon shell, before being able to form a new silicide phase with silicon. The shallow voltage curve is observable in graphite half-cells, too (Figure S4). During the first lithiation, a plateau at around 0.08 V is formed. In this two-phase region c-Si and the formed a-Li_xSi phase coexist.^[16,49] At voltages lower than 0.05 V, a spontaneous phase transition to c-Li₁₅Si₄ takes place.^[16,20,50] The short plateau at 0.44 V during

the following delithiation (charging) indicates the conversion from c-Li₁₅Si₄ to a-Li_xSi.^[49,50] Subsequently, a-Li_xSi is delithiated^[51] so that after the first cycle an amorphization of the silicon takes place,^[20] also confirmed by Raman spectroscopy (Figure S5a). Instead of the sharp peak from c-Si at 520 cm⁻¹ that is observable before cycling, a broader peak at 480 cm⁻¹ originating from amorphous silicon (a-Si) is visible after cycling.^[52] Hence, the following cycles start from a-Si and no potential plateau is formed during lithiation.

In the corresponding cyclic voltammogram (Figure 4b), the small peak at 0.9 V (I) at the beginning of the first cycle originates from reactions of the SE and/or at the Li/SE interface.^[53] During the first lithiation (discharging), the increase of the current density (II) is due to the formation of the Li–Si alloy.^[24] The (de)lithiation of the carbon matrix is visible from the peaks at 0.1 V and 0.14 V (III) during delithiation (charging) in the CV measurement. These peaks arise from the deintercalation of lithium ions from the graphitic domains of the carbon shell.^[54] The peak at 0.465 V (IV) during delithiation corresponds to the short plateau of the voltage curve (Figure 4a). Therefore, this peak matches with the transition from c-Li₁₅Si₄ to a-Li_xSi.^[43,50,55] As mentioned before, beginning from the second cycle the lithiation starts from a-Si and not from c-Si. Subsequently, the shoulder between 0.32 V and 0.13 V (V) builds firstly during the second lithiation. The peak at 0.31 V (VI) and the shoulder at 0.55 V (VII) observable especially

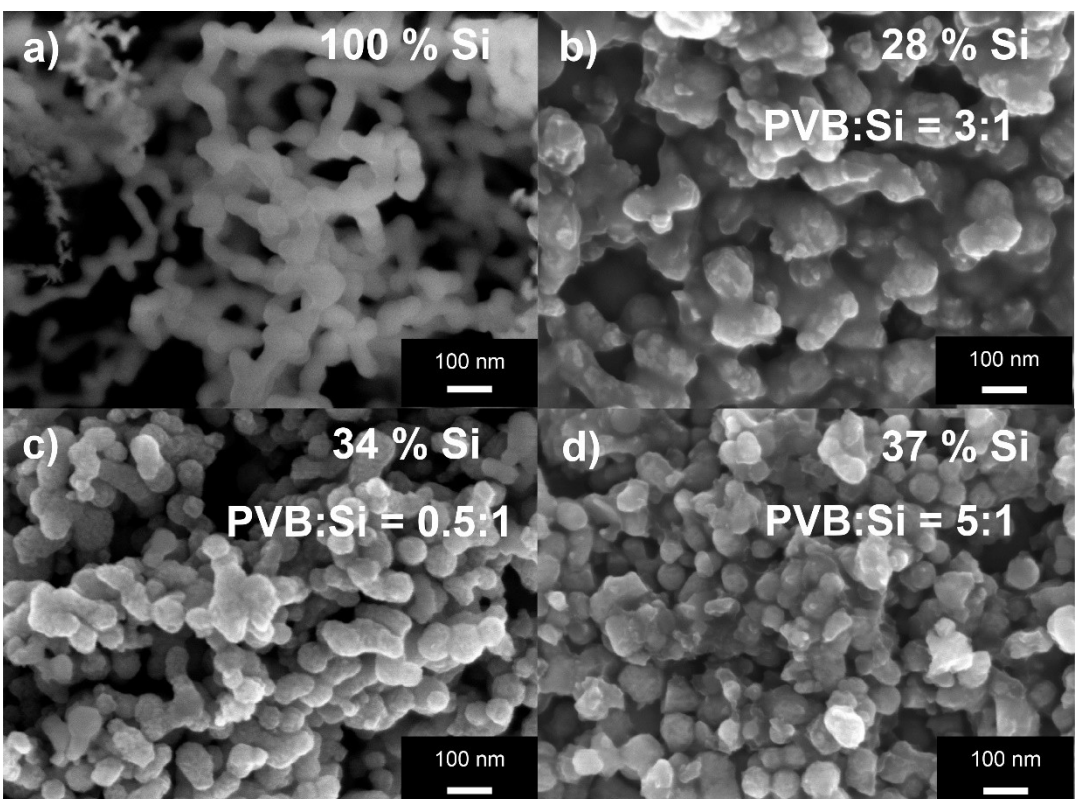


Figure 3. SEM images of bare SiNPs (a) and of the Si–C composites Si28@C (b), Si34@C (c) and Si37@C (d).

during the second and third delithiation can be ascribed to the delithiation of $a\text{-Li}_x\text{Si}$ which has not been transformed to $c\text{-Li}_{15}\text{Si}_4$ during lithiation.^[38,50,55]

The galvanostatic cycle stability of the different Si–C composites in half-cells vs. lithium as well as of the reference active materials were investigated by GCPL using a current density of 0.07 mA cm^{-2} for the first three cycles and 0.2 mA cm^{-2} for the following 50 cycles. For comparison of all materials, the received discharge (lithiation) capacities are referred to the mass of silicon (Figure 4c).

Regarding the half-cells with the Si–C composites containing different Si contents, the half-cell with Si37@C shows the highest lithiation capacities referred to the mass of silicon during all cycles ($> 2570 \text{ mAh g}^{-1}_{\text{Si}}$). The high utilization of silicon can be primarily explained with the highest Si content of Si37@C compared to Si28@C and Si34@C. This is confirmed by the higher current densities in the cyclic voltammogram of the Si37@C|SE|Li cell (Figure 4b) compared to the Si28@C|SE|Li cell (Figure S5b) which are mainly due to the more intensive Si peaks (IV, VI, VII) and correlate with the higher capacities received with GCPL. The ratio between silicon and carbon content is reflected in the intensities of the CV peaks, too, as the peaks from the carbon shell (III) are less intensive during the CV measurement of the Si37@C half-cell.

Comparing the voltage profiles, the curves increase more slowly from Si28@C (Figure S5c) over Si34@C (Figure S5d) to Si37@C (Figure 4a) electrode during delithiation resulting in increasing capacities in this order. Additionally, the comparison

of the lithiation capacities referred to the mass of Si–C composite (active material) shows that the capacities increase with the Si content (Figure S6a). This can be due to increased Si utilization but the (de)lithiation of the carbon matrix also contributes to the received capacities.

As the Si37@C half-cell also exhibits the highest lithiation capacities referred to the mass of Si–C composite ($> 1000 \text{ mAh g}^{-1}_{\text{Si-C}}$ after 53 cycles, Figure S6a), the contacting between SiNPs, CNF and SE particles as well as the size of the voids between SiNPs and carbon matrix (Figure 3d) within the Si37@C electrode seem to be most promising for further evaluation. Additionally, the Si37@C half-cell has the lowest average delithiation (charge) potential resulting in a higher full cell potential and hence higher energy density of the ASSB cells. Besides the lower Si content of Si28@C, the decreased capacity of the Si34@C electrode can be explained with the lower diameter of the Si–C agglomerates (see Figure 3c) leading to a less compact structure, more incomplete contacting between the electrode particles and longer ionic pathways in the solid composite electrode. In addition, the smallest amount of PVB template in the synthesis of Si34@C results in smaller voids that are not large enough with regard to the volume expansion of the SiNPs.

The initial CE (ICE) of Si–C half-cells is remarkably higher for the SE cell (73.2%) compared to the LE cell (45.3%)^[18] due to suppressed SEI formation at the carbon shell. Given to the high applied pressure in the ASSB torque cells, the SEI is also more mechanically stabilized. The liquid electrolyte penetrates the

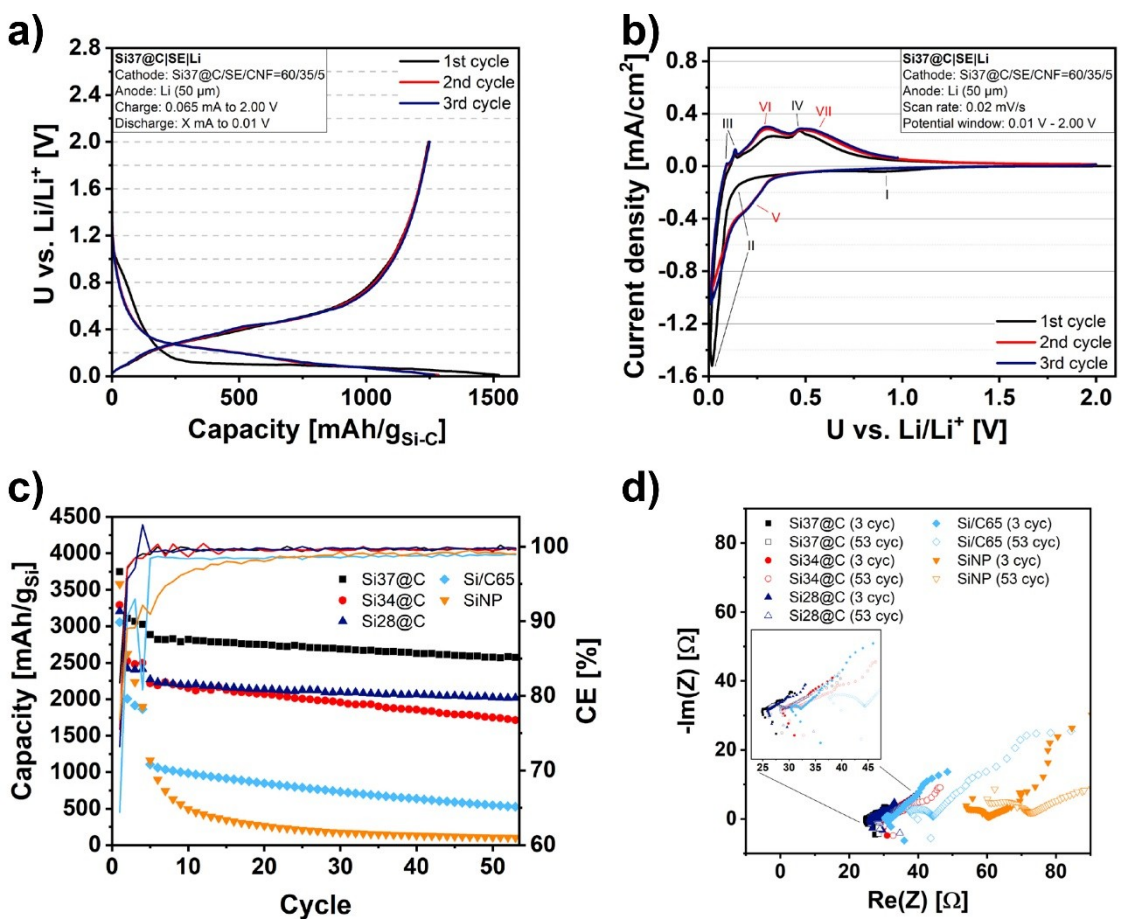


Figure 4. Voltage profiles (a) and cyclic voltammogram (b) of Si37@C|SE|Li half-cell for the first three cycles. Lithiation capacities and coulombic efficiencies (CE) of Si–C, Si/C65 and SiNP half-cells vs. lithium (c) and the corresponding EIS spectra (d) after three and 53 cycles.

whole carbon matrix whereas the SE is in contact with the Si–C particles solely at the outer surface (Figure 1). This also leads to a significantly lower charge transfer resistance (R_{ct} – represented by the diameter of the semicircle) of the SE cell compared to the LE cell, after 3 cycles and especially after 53 cycles (Figure S6b).

The comparison of the cycle stability of the Si–C with the Si/C65 and the pristine SiNP solid-state half-cells shows that the lithiation capacities of the reference cells decrease more rapidly. In the 10th cycle, only 495 mAh g⁻¹_{Si} and 986 mAh g⁻¹_{Si} are received for the SiNP and the Si/C65 half-cell, respectively, whereas the lithiation capacities of the Si–C half-cells lie above 2100 mAh g⁻¹_{Si}. The capacity retentions of the 53rd cycle referred to the fifth cycle are clearly higher for the Si–C composite electrodes (77% to 89%) than for the reference material electrodes (SiNP: 9%, Si/C65: 48%). The high capacity losses of the SiNP and Si/C65 half-cell are due to the structural degradation of the electrode resulting from the volume changes of silicon.^[56] Chen et al.^[57] showed that early-stage defects during lithiation due to inhomogeneities in the SEI cause the mechanical degradation and structural instability of Si electrodes. The resulting contact losses lead to increased charge transfer resistances in the EIS spectra after 53 cycles compared to the EIS spectra after three cycles (Figure 4d). In

contrast, the higher lithiation capacities, the better rate stability and the higher capacity retention of the Si–C half-cells indicate that the volume changes of the SiNPs seem to be well compensated by the carbon shell stabilizing the entire electrode.^[8,56] The diameter of the semicircles in the EIS spectra of the Si–C half-cells is lower and does not significantly change after galvanostatic cycling compared to the reference half-cells (Figure 4d). This indicates both a better maintaining of the contacting between active material and SE particles and also a lower SEI formation. In contrast to the SiNP and Si/C65 electrodes, the SEI formation only takes place at the outer surface of the carbon shell of the Si–C composites without huge volume changes.^[8,56] The carbon shell does not only stabilize the SEI but also increases the electrical conductivity leading to less shifted EIS spectra on the x-axis (Re(Z) axis).^[56] This is already the case when adding carbon nanoparticles in the same mass ratio to SiNPs (Si/C65) as for the best performing Si–C composite Si37@C. However, this mixture is neither capable of buffering the volume changes of the SiNPs nor does the carbon participate in the electrochemistry as can be seen from the voltage profile (Figure S3b) which is similar to the SiNP half-cell. Together with the lower rate and cycle stability of the Si/C65 as well as the SiNP half-cell this proves that the carbon void structure is essential to both compensate volume

changes of the SiNPs and improve the electrochemical utilization.

2.3. Electrochemical Performance of NCM|SE|Si-C Full Cells

NCM|SE|Si-C full cells with different n/p ratios possessing high anode areal loadings of $4.8 \text{ mg}_{\text{Si-C}} \text{ cm}^{-2}$ or 7.4 mAh cm^{-2} were prepared with Si37@C as anode active material and cycled between 1.5 V and 4.25 V. The good Si-utilization and lithiation of the Si37@C electrode in half-cells vs. lithium makes this composite to the material of choice for use in ASSB full cells. The NCM cathode active material ($\text{LiNi}_{0.9}\text{Co}_{0.05}\text{Mn}_{0.05}\text{O}_2$) can achieve a maximum capacity of $207 \text{ mAh g}^{-1}_{\text{NCM}}$, as determined in NCM|SE|Li-In half-cell (Figure S7a). In contrast to half-cells supplying an excess of lithium ions through the lithium metal anode, the amount of lithium ions in full cells is limited by the cathode. Thus, lithium ion losses e.g. due to SEI formation directly influence the cell performance. Additionally, the balancing or n/p ratio plays an important role for lithium-ion full cells describing the ratio between the anode and cathode capacity. On the one hand, n/p ratios lower than one lead to

lithium plating which should be prevented in order to address safety concerns and prolong cycle life. On the other hand, the higher the n/p ratio, the lower the energy density of the cell due to unutilized anode material.^[58,59] In order to prevent lithium plating, n/p ratios greater than one are usually employed.

Regarding the rate performance of a full cell with a Si-C anode oversized by 30% (n/p = 1.3), the discharge capacities decrease with increasing discharge current density from $187 \text{ mAh g}^{-1}_{\text{NCM}}$ at 0.07 mA cm^{-2} to $125 \text{ mAh g}^{-1}_{\text{NCM}}$ at 1.47 mA cm^{-2} (Figure 5a). The lithium ions cannot directly (de)alloy in silicon as they also have to cross the carbon shell. Thus, smaller discharge capacities are observable at high current densities resulting from higher kinetic limitations of the lithium ion diffusion particularly in the Si-C anode compared to NCM|SE|graphite or NCM|SE|Li-In reference cells (Figure S7a and b). The first discharge capacity (Figure 5b) of the NCM|SE|Si-C cell only achieves about 90 to 92% of the discharge capacity of a NCM|SE|Li-In or NCM|SE|graphite reference cell, respectively, which can be increased up to 94 or 95% with an additional constant voltage step (CV step) at the end of discharge (dark blue curve in Figure 5b). Although SEI

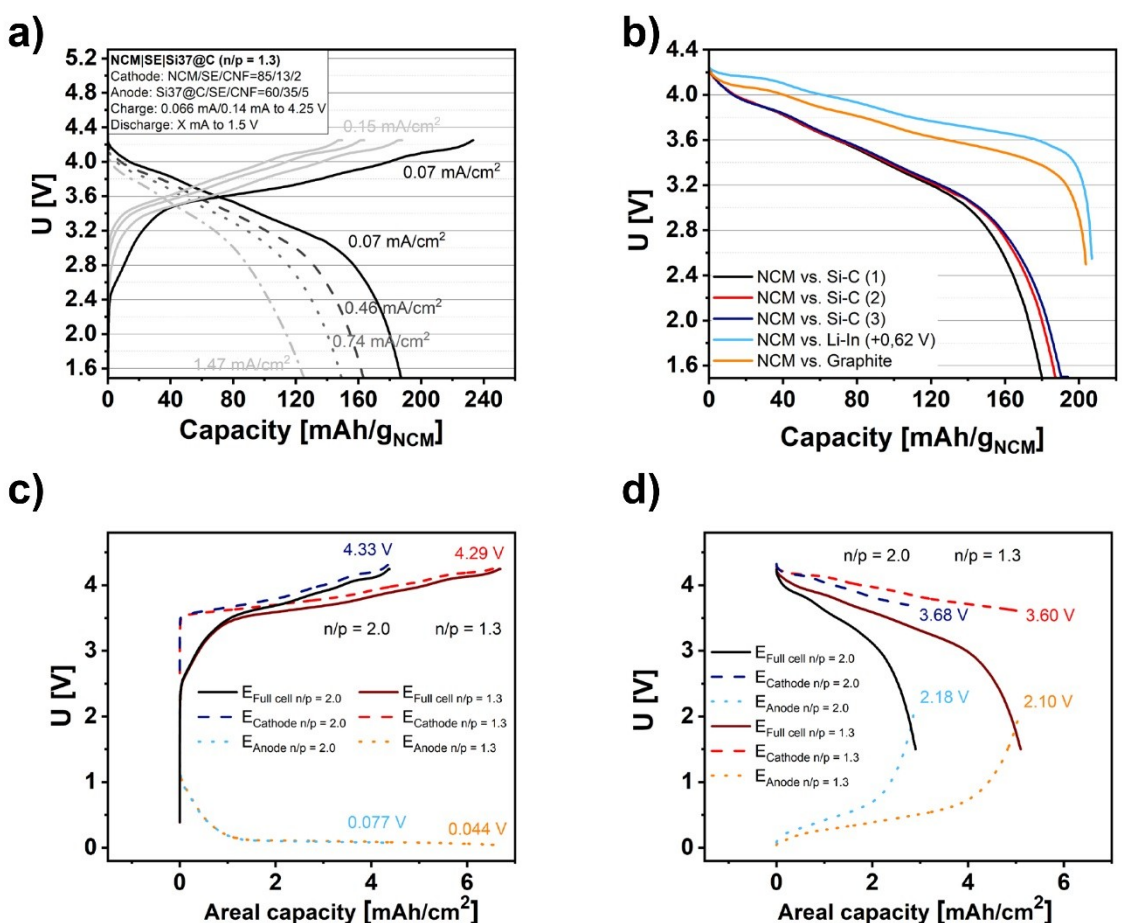


Figure 5. Rate performance of NCM|SE|Si37@C full cell with n/p = 1.3 (a). First discharge profiles of NCM|SE|Si37@C (n/p = 1.3), NCM|SE|Li-In and NCM|SE|graphite (n/p = 1.8) cells with a current density of 0.07 mA cm^{-2} (b). First charge (c) and discharge profiles (d) of 3-electrode NCM|SE|Si37@C full cells with n/p = 1.3 and n/p = 2.0 using lithium as reference electrode (0.07 mA cm^{-2}).

formation and side reactions are significantly reduced in ASSBs, minor irreversible lithium losses are still present. The lowered average voltage during discharge of the NCM|SE|Si-C full cell originates from the flatter descend of the corresponding voltage profile especially above 80% depth of discharge (DOD). The voltage profile of the Si-C half-cell (Figure 4a) near the end of charging is not as steep as of the graphite half-cell (Figure S4) resulting in the flatter voltage curve of the NCM|SE|Si-C full cell near the end of discharge. However, using the Si-C composite as anode material high areal loadings of 7.4 mAh cm^{-2} were realized and the higher volumetric capacity of the anode display a remarkable benefit for designing high-energy full cells.

The slight difference of the discharge capacities between NCM|SE|Si-C cells with the same balancing (Figure 5b) can be ascribed to the different long discharge plateau due to the manual fabrication of the ASSB cells. The resulting various local loadings of the anode can lead to differences in the local C rate as well as in the rate and cycle stability of full cells with the same n/p ratio due to various kinetic limitations.

In order to investigate the influence of the balancing on the full cell performance, NCM|SE|Si-C cells with different n/p ratios were prepared. At first, the anode and cathode potential curves of a cell with a low (1.3) and a high (2.0) n/p ratio was studied with a 3-electrode ASSB setup using lithium as reference electrode since the typical 2-electrode setup only allows measuring the full cell potential. The full cells were fabricated with a constant anode capacity resulting in decreasing cathode capacity with increasing n/p ratio and explaining the difference in areal capacity between low and high overbalancing of the anode (Figure 5c, 5d). After charging (lithiation of the anode) both cells with a current density of 0.07 mA cm^{-2} until 4.25 V (Figure 5c), the anode voltage of the cell with an n/p ratio of 2.0 (0.077 V) lies above the anode potential of the cell with an n/p ratio of 1.3 (0.044 V). The reason for this is the lower utilization and lithiation of the anode with increasing overbalancing of the anode (higher n/p ratio).^[58] For reaching the predefined charge cut-off voltage of the full cell (4.25 V), the cathode potential at the end of charge is higher for the n/p ratio of 2.0 (4.33 V) than for the n/p ratio of 1.3 (4.29 V).^[60] This leads to a higher delithiation of the cathode of the cell with an

n/p ratio of 2.0 which goes along with enhanced structural instability of the cathode.^[58,61] After discharging (lithiation of the cathode) the cells until 1.5 V (Figure 5d), the end potentials of anode and cathode are again higher for the cell with an n/p ratio of 2.0 than for the cell with an n/p ratio of 1.3. The steep increase of the anode potential curve near the end of discharge, observable for both cells, indicate the full delithiation of the Si-C anode. However, the cathodes are not fully lithiated yet at the end of discharge since the end of discharge potential of the cathodes only lies around 3.6 V.^[62] This can be explained with the SEI formation and the corresponding irreversible loss of lithium ions whereby not all lithium ion sites in the NCM lattice can be filled again.^[59] Summarizing, a higher oversizing of the anode (higher n/p ratio) leads to less mechanical stress for the anode but at the same time to higher strain for the cathode. Similar results between low and high overbalancing of the anode were obtained by investigating NCM|LE|Si cells.^[59]

Regarding the rate performance and galvanostatic cycle stability of the NCM|SE|Si-C cells with different n/p ratios, the trends within the first charge capacities and initial coulombic efficiencies (ICE) are considered firstly (Figure 6a). In common with NCM|LE|Si cells,^[59] the first charge capacity of NCM|SE|Si-C cells increases and the corresponding ICE decreases with rising n/p ratio. The increasing end of charge potentials of the cathode at higher overbalancing of the anode and the corresponding higher amount of extracted lithium ions from the cathode lead to the increasing charge capacities. However, as mentioned before, the stronger delithiation also leads to increased structural instability of the cathode. Subsequently, it comes to aggravated and incomplete lithiation of the cathode during discharge, the capacity losses increase and the ICE decreases.^[58,61,63]

Another factor contributing to the decreasing ICE are the dropping cathode capacities – and consequently the amount of available lithium ions in the full cell – with rising n/p ratio. As the same amount of lithium ions is consumed through the SEI formation at the anode for all full cells (by assuming constant anode capacity), the relative capacity loss increases with rising overbalancing of the anode whereby the ICE sinks. This also explains the higher end of discharge potential of the cathode

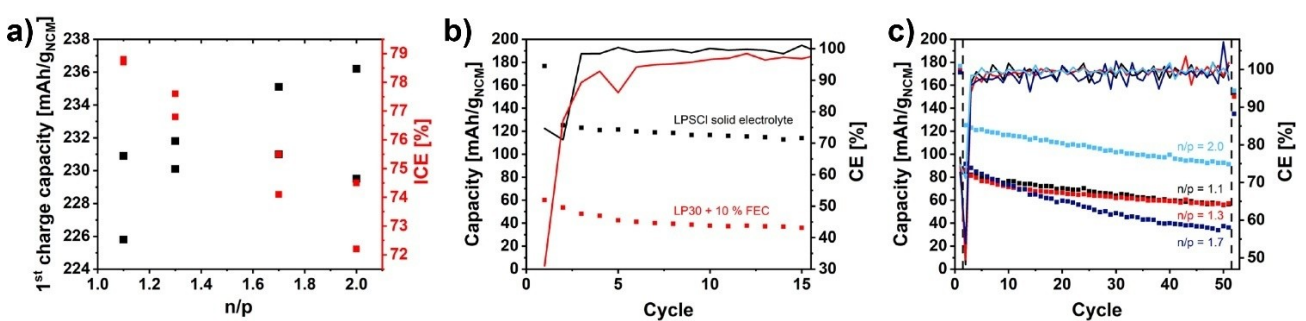


Figure 6. First charge capacities and initial coulombic efficiencies (ICE) of NCM|SE|Si37@C full cells dependent on the n/p ratio (a). Cycle performance of full cells (n/p = 2.0) with liquid and solid electrolyte composed of NCM as cathode and Si-C as anode (b). Discharge capacities and CE of NCM|SE|Si37@C full cells with different n/p ratios (c).

of the full cell with an n/p ratio of 2.0 (3-electrode setup, Figure 5d) as less lithium ions are available to intercalate into the NCM lattice.^[59]

Although the investigation of the rate performance (of 4 cycles) of the NCM|SE|Si-C full cells with different n/p ratios barely reveal differences (Figure S8), more notable trends and differences between various n/p ratios are recognizable through monitoring the galvanostatic cycle stability (Figure 6c).

A clear difference is visible regarding the electrochemical performance of NCM|SE|Si-C and NCM|LE|Si-C full cells (Figure 6b) with the same n/p ratio (note that a different NCM was used in the liquid system to achieve a comparable areal loading in both systems). While the LE cell possess a lower average CE (around 94.7%) due to more continuous SEI formation at the anode, the SE cell delivers a higher average CE (around 99.4%). In addition, the capacity of the SE cell in the 10th cycle ($117 \text{ mAh g}^{-1}_{\text{NCM}}$) is three times as high as the capacity of the LE cell ($38 \text{ mAh g}^{-1}_{\text{NCM}}$). Besides the mechanically stabilized SEI by external pressure in the SE cell, the differences can be mainly explained as following. The solid electrolyte does not penetrate the whole void structure of the Si-C composite in contrast to the liquid electrolyte leading to less electrolyte depletion in the inner parts of the Si-C composite. This also results in a significantly higher ICE of the solid system (72.7%) than for the liquid system (31.0%) since the reduced surface area for SEI formation leads to a lower loss of lithium ions during the first cycle. As a result, NCM|LE|Si-C cells have to be precycled or prelithiated in order to compensate the high initial capacity losses,^[18] which is not necessary for NCM|SE|Si-C cells.

During galvanostatic cycling of the ASSB cells with different n/p ratios, fresh cells were cycled with a low current of 0.07 mA cm^{-2} for charge and discharge of the first (formation) and the last cycle to determine the capacity retention. The cycle stability of the cells was investigated for 50 cycles using 0.2 mA cm^{-2} and 1.0 mA cm^{-2} during charge and discharge, respectively (Figure 6c). Over the 50 cycles, the decreasing discharge capacities (rate performance loss) arise from increasing charge transfer resistances (Figure S9) and the corresponding rising overpotentials. In the last cycle with a low current density as in the first cycle, all cells achieve almost the initial capacity proving the high reversibility of NCM|SE|Si-C cells (Table 2, 78.9%–87.7%). The difference between the capacity of the first (formation) and the last cycle reflects the capacity loss due to irreversible lithium ion losses. The Si-C anode provides higher capacity retentions without the occurrence of short circuits compared to lithium as another high-energy anode

leading to improved safety and enhanced electrochemical performance under ambient conditions.^[28]

Throughout the investigation of the cycle stability of the NCM|SE|Si-C cells over 50 cycles, the cell with an n/p ratio of 1.7 shows the highest overpotential increase as can be seen from the rate performance loss (Table 2, 60.4%) whereas the full cells with a smaller n/p ratio (1.1 and 1.3) show a better performance at higher current rates (Table 2, rate performance loss 33.7%). This devolution of the discharge capacities can be explained with the difference in the end of charge voltage of the cathode. The higher cathode potential of the cell with an n/p ratio of 1.7 leads to faster degradation of the cathode and thus quicker decreasing of the discharge capacities.^[58,63] In contrast, the lower cathode potential of the full cells with smaller overbalancing of the anode (n/p ratio of 1.1 and 1.3) improves the galvanostatic cycle performance. However, the full cell with an n/p ratio of 2.0 deviates from the other cells and shows the highest discharge capacities ($125 \text{ mAh g}^{-1}_{\text{NCM}}$ in the 2nd cycle) with the lowest rate performance loss within the 50 cycles (Table 2, 27.1%) as well as the highest capacity retention (Table 2, 87.7%). The partial lithiation of the Si-C anode at an n/p ratio of 2.0 improves its stability during cycling leading to the high cycle stability of this cell despite the higher cathode potential.^[18] Furthermore, the different behavior of the cell with an n/p ratio of 2.0 compared to the other cells can be explained with the kinetic limitations of the lithium ion diffusion especially in the Si-C anode influencing the cell performance mainly at high current rates.

Summarizing, full cells with a slight (1.1 or 1.3) or a high (2.0) n/p ratio show the best galvanostatic cycling performance regarding discharge capacities and capacity retention whereas the full cell with an n/p ratio of 1.7 shows the highest capacity loss. In addition, estimations of projected energy densities for a unit cell of the cell stack of a multilayered pouch cell (details see supportings) were carried out and compared for two n/p ratios. The higher utilization of the anode at a lower n/p ratio leads to higher projected energy densities (n/p=1.1: 375 Wh kg^{-1} , 1178 Wh l^{-1}) compared to full cells with a larger n/p ratio (n/p=2.0: 297 Wh kg^{-1} , 874 Wh l^{-1}). Thus, an n/p ratio near one is favorable with regard to achievable energy densities.

3. Conclusions

Silicon carbon void structures were demonstrated to be excellent performing anode materials in all-solid-state Li-ion batteries. Outstanding cycling performance in solid-state half- and full cells (capacity retention up to 87.7%) was demonstrated. The void structure enables the lithiation and stable cycling of the silicon material due to a close contact between carbon shell and silicon nanoparticle as well as effective compensation of the volume changes of silicon. This concept leads to higher charging rates at room temperature without short circuits compared to lithium metal anodes. High areal loadings of up to 7.4 mAh cm^{-2} can be reached.

Table 2. Galvanostatic cycle performance (capacity loss between cycle 2 and cycle 51, rate performance loss) and reversibility (capacity retention of cycle 52 vs. cycle 1) of NCM|SE|Si-C full cells with different n/p ratios.

n/p	Rate performance loss (between cycle 2 and cycle 51) [%]	Capacity retention (cycle 52 vs. cycle 1) [%]
1.1	33.6	86.8
1.3	33.8	86.0
1.7	60.4	78.9
2.0	27.1	87.7

The solid-solid interface reduces the active contact area for side reactions and effectively eliminates continuous SEI formation. In addition, the SEI is mechanically stabilized by external pressure. The result is higher capacity retention and ICE compared to liquid electrolyte systems.

Half-cell measurements vs. lithium demonstrated that the volume changes of the SiNPs are compensated through the carbon matrix since all investigated Si–C composites showed higher lithiation capacities, better rate and cycle performance (capacity retention of 77% to 89%) as well as lower cell impedance than the pristine SiNPs (capacity retention of 9%) or SiNPs mixed with carbon nanoparticles (Si/C65, capacity retention of 48%). The composite with the highest Si content of 37% showed the best electrochemical performance ($> 1000 \text{ mAh g}^{-1}_{\text{Si-C}}$ after 53 cycles).

In contrast to liquid electrolyte full cells, the solid-state cells comprising Si–C void structure composites do not require precycling or prelithiation due to their high initial CE. As the SE is not able to penetrate the Si–C void structure like a liquid electrolyte less lithium ions are consumed through SEI formation leading to significantly higher initial discharge capacities and columbic efficiencies compared to the liquid system.

Kinetic limitations in the Si–C composite anode lead to lower discharge capacities of NCM|SE|Si–C full cells at higher current rates. However, decent capacity retention after 50 cycles even at high anode areal loadings as high as 7.4 mAh cm^{-2} were demonstrated.

Using a 3-electrode ASSB cell setup it was shown that a higher n/p ratio of NCM|SE|Si–C full cells leads to stronger delithiation of the cathode as a result of the higher cut-off voltage (lower utilization) of the anode. The investigation of the balancing of NCM|SE|Si–C cells showed that full cells either with a low (1.1 or 1.3) or high (2.0) n/p ratio showed the best electrochemical performance. Regarding the energy density, a lower overbalancing of the anode would be favorable. This report is an important study for balancing of novel anode materials against nickel rich cathodes in all-solid-state batteries. With regard to the increasing demand for high-energy batteries, the herein used silicon carbon void structures present a promising concept for both stabilizing anodes and providing high capacities in ASSBs, which is applicable to any future anode materials suffering from high volume changes.

Experimental Section

Material preparation

For the synthesis of the silicon carbon composites,^[18] 1.0 g SiNPs (Alfa Aesar, 98%, APS $\geq 50 \text{ nm}$) were mixed with Polyvinylbutyral (PVB, B60HH, Mowital) depending on the PVB:Si ratio ($m:m$ 0.5:1, 3:1, 5:1) using a ball mill (MM400, Retsch) for 5 min. Subsequently, the blends were heated at 190°C for 30 min. The obtained Si@PVB composite was ground with the ball mill for 5 min. 2.66 g (PVB:Si ratio 3:1, 3.99 g for 5:1, 1.00 g for 0.5:1) of the ground composite was suspended in 12 ml deionized water and 1 ml ethanol. Subsequently, 3.83 g sucrose (Sigma Aldrich) and 0.27 g of a 2.5 M

sodium hydroxide (Carl Roth) solution were added under stirring. The mixture was heated for 3 h at 100°C and 6 h at 160°C . The ground compound was heated under argon flow with 10 K min^{-1} to 850°C and kept for 2 h. After cooling to 50°C , the obtained Si–C composite was ground again by ball mill. For the Si/C65 mixture, the SiNPs were manually mixed with carbon nanoparticles (C-NERGYTM SUPER C65) using an agate mortar.

The cathode active material, $\text{Li}_2\text{O-ZrO}_2$ (LZO) coated $\text{LiNi}_{0.9}\text{Co}_{0.05}\text{Mn}_{0.05}\text{O}_2$, was prepared by the sol-gel method based on ZrO_2 coating.^[64] The LZO coating sol was synthesized from 2-propanol, lithium methoxide (equivalent of 10 wt%-lithium methoxide in methanol solution) and zirconium (IV) tetrapropoxide ($\text{Zr}(\text{OC}_3\text{H}_7)_4$) in the molar ratio 200:2:1. NCM ($\text{LiNi}_{0.9}\text{Co}_{0.05}\text{Mn}_{0.05}\text{O}_2$) was dispersed in this solution and stirred for 1 h. The 2-propanol was evaporated under vacuum at 50°C (water bath) while undergoing ultrasonic treatment in order to avoid aggregation of NCM particles. After filtration, the precursor was heated at 350°C for 1 h under air, and the LZO coated NCM was obtained. The crystal structure of NCM did not change even after the coating procedure and was found to be $\alpha\text{-NaFeO}_2$ with $R\bar{3}m$ space group. A uniform, (X-Ray) amorphous LZO coating with a thickness of $\sim 3.8 \text{ nm}$ has formed (see supportings in Cangaz et al.^[28]).

The solid crystalline electrolyte $\text{Li}_6\text{PS}_5\text{Cl}$ was prepared by mechanical milling with high purity (see supportings in Cangaz et al.^[28]) in accordance to the previous publications (Figure S10).^[65] Determined amounts of Li_2S (Alfa Aesar, 99%), LiCl (Alfa Aesar, 99%) and P_2S_5 (Sigma-Aldrich Co., 99%) were weighed and mixed in an agate mortar for about 20 min, then transferred in a zirconia (Zr) bowl with Zr spheres (10mmφ) and sealed in an argon filled box. High-energy ball milling was conducted by using the planetary mill P5 (Fritsch, Germany) for 16.5 h with a rotational velocity of 380 rpm. After the milling, the mixture powder was wrapped in a gold foil and placed in a carbon crucible. The carbon crucible was put into a quartz tube and the tube was then vacuum sealed. Using a muffle furnace, the quartz tube was heated at 550°C for 1 h. After the heat treatment, the quartz tube was cooled down to room temperature.^[28]

Electrode preparation

The powdered cathode composite electrode was prepared by mixing the active material NCM (AM), conductive carbon additive (vapor-grown carbon nanofibers, VG-CNF), and solid electrolyte ($\text{Li}_6\text{PS}_5\text{Cl}$, SE, particle size 1–2 μm ^[28]) in the mass ratio of 85:13:2. For the preparation of the powdered anode composite electrodes the active material (Si–C, SiNPs, Si/C65), the VG-CNF and the SE (particle size 3–4 μm ^[28]) were mixed in the ratio of 60:35:5 for 30 min in an agate mortar by hand.

The Si–C anodes used with liquid electrolyte were prepared based on a water based slurry. The slurry contained 80 wt% Si–C, 10 wt% multiwalled carbon nanotubes (MWCNT, Nanocyl7000, 90%) and 10 wt% styrene-butadiene rubber (SBR, Targray, 15%) and was blended with a mixer mill (MM400, Retsch) at 25 Hz for 15 min. After coating on a copper foil (9 μm) with an automatic film applicator (BYK), the coatings were dried at 80°C for 2 h. The resulting Si–C anodes have a density of 0.6 g cm^{-3} and a loading of 4.3–4.8 mg cm^{-2} .

Preparation of a test cell

Test cells were prepared in half- and full cell configurations for investigating the basic characteristics of cathode and anode such as the charge/discharge potential profiles, rate discharge capability and the cell internal resistance.

The ASSB cells were prepared by using a die with a diameter of 13 mm as described previously.^[64] The cell comprises of a stainless steel outer casing with a Teflon liner. For a typical test cell, 150 mg (~750 µm) of the electrolyte Li₆PS₅Cl powder (particle size 3–4 µm^[28]) was uniformly spread inside the die by a micro-spatula. Next, the powder was once temporally compressed and compacted into a pellet.

For half-cells, the anode composite powder (Si28@C, Si34@C, Si37@C, Si/C65, SiNP) or cathode composite powder was homogeneously distributed across the compacted electrolyte surface in the die. Then the electrode layer was temporarily compressed. On the opposite side of the cell stack, a lithium or lithium-indium anode (Li–In) was placed and compressed as described by Takada et al.^[66]

For NCM|SE|Si–C full cells, 7.64 mg of the anode composite (Si37@C) and the respective amount of the cathode composite, according to the n/p ratio (1.1, 1.3, 1.7, 2.0), were homogeneously distributed on opposite sides of the compacted electrolyte surface. For the balancing of the full cells, the first cycle practical specific lithiation capacity of the composite anode (922 mAh g⁻¹) and the first cycle practical specific discharge capacity of the cathode (176 mAh g⁻¹), based on the half-cell characterization, were used for the calculation of the areal capacities and loadings.

Then, all the cell components were again pressed together and completely pelletized by using a hydraulic press (300 MPa for 30 s were applied). After compression, the cell stack was placed inside the outer steel casing where a screw maintains the electric contact in the cell. The screw was fastened at 3.5 Nm using a preset torque.

The Si–C electrodes used with liquid electrolyte in coin cells were dried at 80 °C under vacuum for 12 h. For half-cells, the Si–C electrodes (diameter 12 mm) were tested vs. a lithium anode (99.9%, diameter 16.5 mm, 250 µm thick, MTI Corporation). The full cells contained a Si–C anode (diameter 16 mm) and a NCM111 cathode (diameter 15 mm). CR2016 coin cells (MTI Corp.) were assembled with the Al₂O₃ impregnated polyethylene terephthalate separator FS3002 by Freudenberg (diameter 19 mm, 22 µm thick), a stainless steel spacer (1 mm thick) and 30 µl (half-cells) or 50 µl (full cells) LP30 + 10% fluoroethylene carbonate (FEC). LP30 (99.9%, Solvionic SA) contains 1 M lithium hexafluorophosphate (LiPF₆) in 1:1 (v/v) ethylene carbonate and dimethyl carbonate.

All above mentioned processes were carried out in an Ar filled glove box (<0.1 ppm H₂O and O₂).

Characterization

The powder X-ray diffraction (XRD, CuKα, 40 kV, 40 mA) pattern was measured using a D5005 XRD system (Siemens, Germany) for verifying crystallinity of Si–C anodes and crystalline side products of the syntheses at room temperature.

Raman measurements were conducted to analyze the crystalline or amorphous Si–C anodes using a Raman microscope (micro-Raman Spectrometer, Renishaw inVia PLC) with an excitation laser wavelength of 514 nm and a 50× lens. The laser beam power at the specimen was 10% and the acquisition time was 5×60 s. For XRD and Raman measurements Kapton tape (3 M) was used to prevent degradation due to moisture.

The scanning electron microscope (SEM) JSM-7800F from JEOL with an Upper Electron Detector (UED) inlense detector and 3 kV acceleration voltage was used to analyze the structure of the different Si–C and the SiNPs. The average size of the particles was determined by measuring the diameter of ten particles with the program ImageJ which then calculated the average value and the standard deviation. Transmission electron microscope (TEM) im-

ages of the Si–C were obtained with a JEM-2100 from JEOL (200 kV acceleration voltage).

To quantify the silicon content of the Si–C a Netzsch STA 409 PC/PG simultaneous thermal analyzer was used. A specific amount of a Si–C sample was heated under argon with 10 K min⁻¹ to 500 °C and held for 30 min and heated again with 5 K min⁻¹ to 1000 °C and held for 30 min. Assuming that the Si particles are fully oxidized to SiO₂ due to the heat treatment the Si content can be calculated from the ratio between the mass of silicon and the mass of the sample. The mass of silicon is calculated from the mass of the SiO₂ residue and the ratio between the molar masses of Si and SiO₂. The average value of three measurements for each sample was determined.

The investigation of the voltage profiles, rate and cycle stability of the half- and full cells via galvanostatic cycling with potential limitation (GCPL) were conducted with a battery tester CTS-lab (BaSyTec, Germany) at 25 °C. Cyclic voltammetry (CV) and electrochemical impedance (EIS) were measured with a VMP-3 (Bio-Logic, France) controlled by a computer. The EIS measurements were conducted with an amplitude of 10 mV in a frequency range of 0.1 Hz–1 MHz at 25 °C.

Acknowledgements

Open access funding enabled and organized by Projekt DEAL.

Conflict of Interest

The authors declare no conflict of interest.

Keywords: all-solid-state battery • balancing • nanostructures • silicon carbon composites • thiophosphate solid electrolyte

- [1] a) D. Larcher, J.-M. Tarascon, *Nat. Chem.* **2015**, *7*, 19; b) T. Pohl, G. Heweling, C. Fischer, K. Weber, *Int. J. Environ. Sci.* **2017**, *2*, 410.
- [2] D. Andre, S.-J. Kim, P. Lamp, S. F. Lux, F. Maglia, O. Paschos, B. Stiaszny, *J. Mater. Chem. A* **2015**, *3*, 6709.
- [3] N. Nitta, F. Wu, J. T. Lee, G. Yushin, *Mater. Today* **2015**, *18*, 252.
- [4] X. Su, Q. Wu, J. Li, X. Xiao, A. Lott, W. Lu, B. W. Sheldon, J. Wu, *Adv. Energy Mater.* **2014**, *4*, 1300882.
- [5] R. Schmuck, R. Wagner, G. Hörpel, T. Placke, M. Winter, *Nat. Energy* **2018**, *3*, 267.
- [6] H. Wu, Y. Cui, *Nano Today* **2012**, *7*, 414.
- [7] L. Li, S. Li, Y. Lu, *Chem. Commun.* **2018**, *54*, 6648.
- [8] J. Wang, T. Xu, X. Huang, H. Li, T. Ma, *RSC Adv.* **2016**, *6*, 87778.
- [9] X. Zhang, D. Kong, X. Li, L. Zhi, *Adv. Funct. Mater.* **2019**, *29*, 1806061.
- [10] a) L. Baggetto, R. A. H. Niessen, F. Rooseboom, P. H. L. Notten, *Adv. Funct. Mater.* **2008**, *18*, 1057; b) Y. S. Jung, D. Y. Oh, Y. J. Nam, K. H. Park, *Isr. J. Chem.* **2015**, *55*, 472.
- [11] J. Janek, W. G. Zeier, *Nat. Energy* **2016**, *1*, 1167.
- [12] N. Liu, W. Li, M. Pasta, Y. Cui, *Front. Phys.* **2014**, *9*, 323.
- [13] a) F. Han, A. S. Westover, J. Yue, X. Fan, F. Wang, M. Chi, D. N. Leonard, N. J. Dudney, H. Wang, C. Wang, *Nat. Energy* **2019**, *4*, 187; b) F. Han, J. Yue, X. Zhu, C. Wang, *Adv. Energy Mater.* **2018**, *8*, 1703644.
- [14] T. Krauskopf, H. Hartmann, W. G. Zeier, J. Janek, *ACS Appl. Mater. Interfaces* **2019**, *11*, 14463.
- [15] Y.-G. Lee, S. Fujiki, C. Jung, N. Suzuki, N. Yashiro, R. Omoda, D.-S. Ko, T. Shiratsuchi, T. Sugimoto, S. Ryu, J. H. Ku, T. Watanabe, Y. Park, Y. Aihara, D. Im, I. T. Han, *Nat. Energy* **2020**, *3*, 267.
- [16] D. Ma, Z. Cao, A. Hu, *Nano-Micro Lett.* **2014**, *6*, 347.
- [17] a) N. Nitta, G. Yushin, *Part. Part. Syst. Charact.* **2014**, *31*, 317; b) M. N. Obrovac, L. Christensen, *Electrochim. Solid-State Lett.* **2004**, *7*, A93.

- [18] A. Baasner, F. Reuter, M. Seidel, A. Krause, E. Pflug, P. Härtel, S. Dörfler, T. Abendroth, H. Althues, S. Kaskel, *J. Electrochem. Soc.* **2020**, *167*, 020516.
- [19] M. Slovick, "Tesla Battery Day – Taking EVs to the Next Level", can be found under <https://www.electronicdesign.com/markets/automotive/article/21143628/tesla-battery-day-taking-evs-to-the-next-level>, **2020**.
- [20] M. Ashuri, Q. He, L. L. Shaw, *Nanoscale* **2016**, *8*, 74.
- [21] X. H. Liu, L. Zhong, S. Huang, S. X. Mao, T. Zhu, J. Y. Huang, *ACS Nano* **2012**, *6*, 1522.
- [22] a) J. Xu, Q. Zhang, Y.-T. Cheng, *J. Electrochem. Soc.* **2016**, *163*, A401-A405; b) M. Ge, J. Rong, X. Fang, A. Zhang, Y. Lu, C. Zhou, *Nano Res.* **2013**, *6*, 174.
- [23] a) V. Chakrapani, F. Rusli, M. A. Filler, P. A. Kohl, *J. Power Sources* **2012**, *205*, 433; b) H. Chen, Y. Xiao, L. Wang, Y. Yang, *J. Power Sources* **2011**, *196*, 6657.
- [24] C. K. Chan, H. Peng, G. Liu, K. McIlwrath, X. F. Zhang, R. A. Huggins, Y. Cui, *Nat. Nanotechnol.* **2008**, *3*, 31.
- [25] a) A. T. Tesfaye, R. Gonzalez, J. L. Coffer, T. Djenizian, *ECS Trans.* **2017**, *77*, 349; b) J. Ha, U. Paik, *J. Power Sources* **2013**, *244*, 463; c) H. Wu, G. Chan, J. W. Choi, I. Ryu, Y. Yao, M. T. McDowell, S. W. Lee, A. Jackson, Y. Yang, L. Hu, Y. Cui, *Nat. Nanotechnol.* **2012**, *7*, 310.
- [26] a) J. W. Wang, Y. He, F. Fan, X. H. Liu, S. Xia, Y. Liu, C. T. Harris, H. Li, J. Y. Huang, S. X. Mao, T. Zhu, *Nano Lett.* **2013**, *13*, 709; b) C. Yu, X. Li, T. Ma, J. Rong, R. Zhang, J. Shaffer, Y. An, Q. Liu, B. Wei, H. Jiang, *Adv. Energy Mater.* **2012**, *2*, 68.
- [27] M. Piwko, S. Thieme, C. Weller, H. Althues, S. Kaskel, *J. Power Sources* **2017**, *362*, 349.
- [28] S. Cangaz, F. Hippauf, F. S. Reuter, S. Doerfler, T. Abendroth, H. Althues, S. Kaskel, *Adv. Energy Mater.* **2020**, *3*, 2001320.
- [29] a) S. Chen, M. L. Gordin, R. Yi, G. Howlett, H. Sohn, D. Wang, *Phys. Chem. Chem. Phys.* **2012**, *14*, 12741; b) G. X. Wang, J. H. Ahn, J. Yao, S. Bewlay, H. K. Liu, *Electrochem. Commun.* **2004**, *6*, 689; c) N. Liu, H. Wu, M. T. McDowell, Y. Yao, C. Wang, Y. Cui, *Nano Lett.* **2012**, *12*, 3315; d) W. Wang, I. Ruiz, K. Ahmed, H. H. Bay, A. S. George, J. Wang, J. Butler, M. Ozkan, C. S. Ozkan, *Small* **2014**, *10*, 3389; e) T. Mori, C.-J. Chen, T.-F. Hung, S. G. Mohamed, Y.-Q. Lin, H.-Z. Lin, J. C. Sung, S.-F. Hu, R.-S. Liu, *Electrochim. Acta* **2015**, *165*, 166.
- [30] a) J. Shi, L. Zu, H. Gao, G. Hu, Q. Zhang, *Adv. Funct. Mater.* **2020**, *13*, 2002980; b) K. McCormac, I. Byrd, R. Brannen, B. Seymour, J. Li, J. Wu, *Phys. Status Solidi A* **2015**, *212*, 877.
- [31] a) B. D. Polat, O. Keles, *J. Alloys Compd.* **2015**, *622*, 418; b) X. Wang, L. Sun, X. Hu, R. A. Susantyoko, Q. Zhang, *J. Power Sources* **2015**, *280*, 393.
- [32] Y. Yao, N. Liu, M. T. McDowell, M. Pasta, Y. Cui, *Energy Environ. Sci.* **2012**, *5*, 7927.
- [33] a) L. Chen, K. Wang, X. Xie, J. Xie, *Electrochem. Solid-State Lett.* **2006**, *9*, A512; b) H. Guo, H. Zhao, C. Yin, W. Qiu, *Mater. Sci. Eng. B* **2006**, *131*, 173; c) I. Kovalenko, B. Zdyrko, A. Magasinski, B. Hertzberg, Z. Milicev, R. Burtovyy, I. Luzinov, G. Yushin, *Science* **2011**, *334*, 75.
- [34] a) S. Dalavi, P. Guduru, B. L. Lucht, *J. Electrochem. Soc.* **2012**, *159*, A642-A646; b) A. M. Haregewoin, A. S. Wotango, B.-J. Hwang, *Energy Environ. Sci.* **2016**, *9*, 1955.
- [35] X. Huang, *J. Solid State Electrochem.* **2011**, *15*, 649.
- [36] C. Cao, Z.-B. Li, X.-L. Wang, X.-B. Zhao, W.-Q. Han, *Front. Energy Res.* **2014**, *2*, 947.
- [37] J. Sakabe, N. Ohta, T. Ohnishi, K. Mitsuishi, K. Takada, *Commun. Chem.* **2018**, *1*, 13.
- [38] R. Miyazaki, N. Ohta, T. Ohnishi, I. Sakaguchi, K. Takada, *J. Power Sources* **2014**, *272*, 541.
- [39] R. Okuno, M. Yamamoto, Y. Terauchi, M. Takahashi, *Energy Procedia* **2019**, *156*, 183.
- [40] N. Ohta, S. Kimura, J. Sakabe, K. Mitsuishi, T. Ohnishi, K. Takada, *ACS Appl. Mater. Interfaces* **2019**, *2*, 7005.
- [41] J. C. Bachman, S. Muy, A. Grimaud, H.-H. Chang, N. Pour, S. F. Lux, O. Paschos, F. Maglia, S. Lupart, P. Lamp, L. Giordano, Y. Shao-Horn, *Chem. Rev.* **2016**, *116*, 140.
- [42] A. Sakuda, A. Hayashi, M. Tatsumisago, *Curr. Opin. Electrochem.* **2017**, *6*, 108.
- [43] K.-B. Kim, N. A. Dunlap, S. S. Han, J. J. Jeong, S. C. Kim, K. H. Oh, S.-H. Lee, *J. Electrochem. Soc.* **2018**, *165*, A1903–A1908.
- [44] A. Baasner, S. Dörfler, M. Piwko, S. Desilani, J. Brückner, H. Althues, S. Kaskel, *J. Mater. Chem. A* **2018**, *6*, 14787.
- [45] a) H. Xu, B. Gao, H. Cao, X. Chen, L. Yu, K. Wu, L. Sun, X. Peng, J. Fu, *J. Nanomat.* **2014**, *2014*, *1*; b) Y. Utsumi, M. Yamakata, T. Kikegawa, O. Shimomura, *Phys. Rev. B* **1992**, *46*, 6031.
- [46] B. Li, D. Yu, S.-L. Zhang, *Phys. Rev. B* **1999**, *59*, 1645.
- [47] A. Käppler, F. Windrich, M. G. J. Löder, M. Malanin, D. Fischer, M. Labrenz, K.-J. Eichhorn, B. Voit, *Anal. Bioanal. Chem.* **2015**, *407*, 6791.
- [48] a) L. Zou, B. Huang, Y. Huang, Q. Huang, C. Wang, *Mater. Chem. Phys.* **2003**, *82*, 654; b) A. C. Ferrari, *Solid State Commun.* **2007**, *143*, 47.
- [49] J. Li, J. R. Dahn, *J. Electrochem. Soc.* **2007**, *154*, A156.
- [50] K. Ogata, E. Salager, C. J. Kerr, A. E. Fraser, C. Ducati, A. J. Morris, S. Hofmann, C. P. Grey, *Nat. Commun.* **2014**, *5*, 3217.
- [51] M. N. Obrovac, V. L. Chevrier, *Chem. Rev.* **2014**, *114*, 11444.
- [52] K. O. Bugaev, A. A. Zelenina, V. A. Volodin, *Int. J. Spectrosc.* **2012**, *2012*, *1*.
- [53] S. Boulineau, M. Courty, J.-M. Tarascon, V. Viallet, *Solid State Ionics* **2012**, *221*, 1.
- [54] a) M. D. Levi, D. Aurbach, *J. Phys. Chem. B* **1997**, *101*, 4630; b) B. Markovsky, M. D. Levi, D. Aurbach, *Electrochim. Acta* **1998**, *43*, 2287.
- [55] T. D. Hatchard, J. R. Dahn, *J. Electrochem. Soc.* **2004**, *151*, A838.
- [56] X. Xiao, W. Zhou, Y. Kim, I. Ryu, M. Gu, C. Wang, G. Liu, Z. Liu, H. Gao, *Adv. Funct. Mater.* **2015**, *25*, 1426.
- [57] C. Chen, T. Zhou, D. L. Danilov, L. Gao, S. Benning, N. Schön, S. Tardif, H. Simons, F. Hausen, T. U. Schülli, R.-A. Eichel, P. H. L. Notten, *Nat. Commun.* **2020**, *11*, 3283.
- [58] J. Kasnatscheew, T. Placke, B. Streipert, S. Rothermel, R. Wagner, P. Meister, I. C. Laskovic, M. Winter, *J. Electrochem. Soc.* **2017**, *164*, A2479–A2486.
- [59] F. Reuter, A. Baasner, J. Pampel, M. Piwko, S. Dörfler, H. Althues, S. Kaskel, *J. Electrochem. Soc.* **2019**, *166*, A3265–A3271.
- [60] S. D. Beattie, M. J. Loveridge, M. J. Lain, S. Ferrari, B. J. Polzin, R. Bhagat, R. Dashwood, *J. Power Sources* **2016**, *302*, 426.
- [61] J. Kasnatscheew, M. Evertz, B. Streipert, R. Wagner, S. Nowak, I. C. Laskovic, M. Winter, *J. Phys. Chem. C* **2017**, *121*, 1521.
- [62] H.-J. Noh, S. Youn, C. S. Yoon, Y.-K. Sun, *J. Power Sources* **2013**, *233*, 121.
- [63] a) J. Kasnatscheew, R. Wagner, M. Winter, I. Cekic-Laskovic, *Top. Curr. Chem.* **2018**, *376*, 16; b) A. O. Kondrakov, H. Geßwein, K. Galdina, L. de Biasi, V. Meded, E. O. Filatova, G. Schumacher, W. Wenzel, P. Hartmann, T. Brezesinski, J. Janek, *J. Phys. Chem. C* **2017**, *121*, 24381.
- [64] S. Ito, S. Fujiki, T. Yamada, Y. Aihara, Y. Park, T. Y. Kim, S.-W. Baek, J.-M. Lee, S. Doo, N. Machida, *J. Power Sources* **2014**, *248*, 943.
- [65] P. R. Rayavarapu, N. Sharma, V. K. Peterson, S. Adams, *J. Solid State Electrochem.* **2012**, *16*, 1807.
- [66] K. Takada, *Solid State Ionics* **1996**, *86*–88, 877.

Manuscript received: February 24, 2021

Revised manuscript received: April 13, 2021

Accepted manuscript online: April 20, 2021

Version of record online: May 6, 2021